New software protocols for enabling laboratory based temporal CT

Parmesh Gajjar,[1,a)] Jakob S. Jørgensen,[1,2] Jose R. A. Godinho,[1,3] Chris G. Johnson,[2,4] Andrew Ramsey,[5] and Philip J. Withers[1,6]

[1]*Henry Moseley X-Ray Imaging Facility, School of Materials, The University of Manchester, Oxford Road, Manchester M13 9PL, United Kingdom*
[2]*School of Mathematics, The University of Manchester, Oxford Road, Manchester M13 9PL, United Kingdom*
[3]*Helmholtz-Zentrum Dresden-Rossendorf, Helmholtz Institute Freiberg for Resource Technology, Chemnitzer Strasse 40, 09599 Freiberg, Germany*
[4]*Manchester Centre for Nonlinear Dynamics, The University of Manchester, Oxford Road, Manchester M13 9PL, United Kingdom*
[5]*Nikon Metrology Inc., 12701 Grand River Avenue, Brighton, Michigan 48116, USA*
[6]*Henry Royce Institute, The University of Manchester, Oxford Road, Manchester M13 9PL, United Kingdom*

Temporal micro-computed tomography (CT) allows the non-destructive quantification of processes that are evolving over time in 3D. Despite the increasing popularity of temporal CT, the practical implementation and optimisation can be difficult. Here, we present new software protocols that enable temporal CT using commercial laboratory CT systems. The first protocol drastically reduces the need for periodic intervention when making time-lapse experiments, allowing a large number of tomograms to be collected automatically. The automated scanning at regular intervals needed for uninterrupted time-lapse CT is demonstrated by analysing the germination of a mung bean (*vigna radiata*), whilst the synchronisation with an *in situ* rig required for interrupted time-lapse CT is highlighted using a shear cell to observe granular segregation. The second protocol uses golden-ratio angular sampling with an iterative reconstruction scheme and allows the number of projections in a reconstruction to be changed as sample evolution occurs. This overcomes the limitation of the need to know *a priori* what the best time window for each scan is. The protocol is evaluated by studying barite precipitation within a porous column, allowing a comparison of spatial and temporal resolution of reconstructions with different numbers of projections. Both of the protocols presented here have great potential for wider application, including, but not limited to, *in situ* mechanical testing, following battery degradation and chemical reactions. *Published by AIP Publishing.* https://doi.org/10.1063/1.5044393

I. INTRODUCTION

X-ray micro-computed tomography (CT) has grown into a popular tool for non-destructively examining the interior of objects to micron scale resolutions, with excellent reviews of the broad range of applications across material science,[1] food technology,[2] biology,[3] and geosciences.[4,5] With off-the-shelf commercial micro-CT machines available for as little as 60 000 Euros, it has also become a widely accessible laboratory technique with an estimated 2000-3000 machines worldwide.[6] Maximising the scientific potential of these laboratory machines is thus of high value.

While many of these machines are used for static 3D observation of materials, they are being increasingly deployed for temporal studies.[7] As a non-destructive technique, CT can be used to repeatedly acquire 3D images and thereby follow changes to the internal structure of materials and components during their manufacture (e.g., additive manufacturing[8] and powder processing[9]) or whilst they are performing in service (e.g., under stress[10] or during cracking[11] and fracture[12]).

In a dynamic process, the sample can be changed constantly and so the relationship between the scan time and the rate of evolution of the sample is important. In practice, the time taken for a CT scan is determined by the time needed to acquire a sufficient number of projections of the sample viewed from different angles as it is irradiated with x-rays. These projections can then be reconstructed into a virtual volume known as a tomogram. Although synchrotron facilities (frame rates up to 10 000 projections/s)[13] and medical CT scanners (frame rates up to 10 projections/s)[14] can perform fast scans, the scan times for laboratory machines are typically much longer ($\sim$1 s–10 min per projection).[15] These time scales give rise to two strategies for data acquisition for *in situ* temporal CT:[16] (1) "Time-lapse CT," which is directly analogous to time-lapse photography, involves collecting a series of bursts of projections, where each burst is collected over a time scale that is short relative to the whole process, and (2) "Continuous streaming," where projections are continuously acquired whilst the sample evolves. *In situ* time-lapse CT can be further categorised into "interrupted" and "uninterrupted." In the former case, the process governing the evolution of the sample is "interrupted" (paused) whilst a scan is acquired.[17] In the latter case, the acquisition time is much shorter than the evolution time, allowing scans to be performed at specific points but leaving the evolution "uninterrupted."[18] Finally, when the rate of evolution of the sample is comparable to the scan time, a continuous acquisition of projections is

---

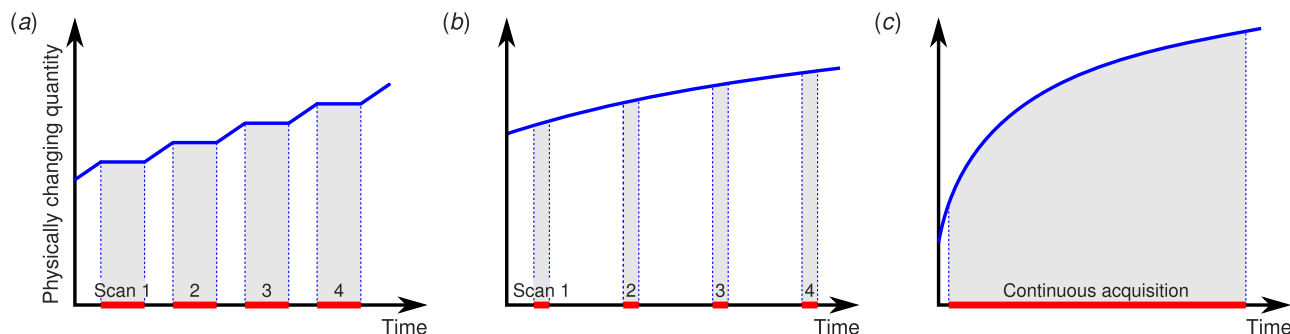a)Electronic mail: parmesh.gajjar@alumni.manchester.ac.uk

FIG. 1. The relationship between the evolution of the sample (blue curves) with the scan time (red) leads to different temporal CT modes, after Ref. 16: (a) Interrupted time-lapse CT, (b) uninterrupted time-lapse CT, and (c) continuous streaming CT. In this paper, we implement protocols for both interrupted and uninterrupted time-lapse CT and for continuous streaming on commercial machines. Each protocol is demonstrated with examples of granular segregation, the germination of a mung bean, and mineral precipitation in a porous column, respectively.

required. These different temporal scan modes are illustrated in Fig. 1.

Of course, the longer scan times associated with laboratory CT are directly related to the lower flux typical of laboratory tube x-ray sources, meaning that longer exposure times are needed to accumulate sufficient photons on the detector for a high signal-to-noise ratio in the projection images. Other technological limitations, such as detector efficiency and performance of add-on-equipment, were recently reviewed by Bultreys *et al.*[19] Together, these limitations present a significant barrier to using laboratory CT machines to study dynamic processes since they place an upper limit on the rate of evolution that can be examined. Even for relatively slow processes where the acquisition rates of laboratory CT systems are well tuned to the time scales of the processes being followed, they are still under-utilised. Limited work has been done, for example, in the areas of root growth[20] and degradation of construction materials,[21] but there is certainly untapped potential.

One significant additional challenge faced by many laboratory users arises from the proprietary software used to control commercial machines. Each manufacturer provides a user interface which includes utilities such as calibration and beam warming, along with routines that guide the user through configuring and starting their scan. While such proprietary software has lowered the barriers to new applications of static CT, it presents an obstacle for temporal studies. Starting a new scan requires user intervention, which becomes impractical when wanting to undertake a large number of scans. Figure 2 summarises laboratory-based temporal studies identified by the authors to date according to the number of tomograms in a time-series, the temporal scanning mode, and the machine type. The above impracticality of conducting a large number of scans could explain why all but 8 of the 60+ time-lapse studies (both interrupted and uninterrupted) are limited to less than 10 tomograms in a time-series with none acquiring more than 30. A number of groups have developed custom CT machines in-house by assembling individual x-ray sources, manipulators, and detectors. These afford a greater degree of flexibility over commercial machines[22] and have allowed the implementation of continuous streaming.[23,24] However, as shown in Fig. 2, continuous acquisition has not yet been implemented on a commercial machine.

Usually for both time-lapse and continuous streaming, the number of projections N for each scan is decided *ex ante*,
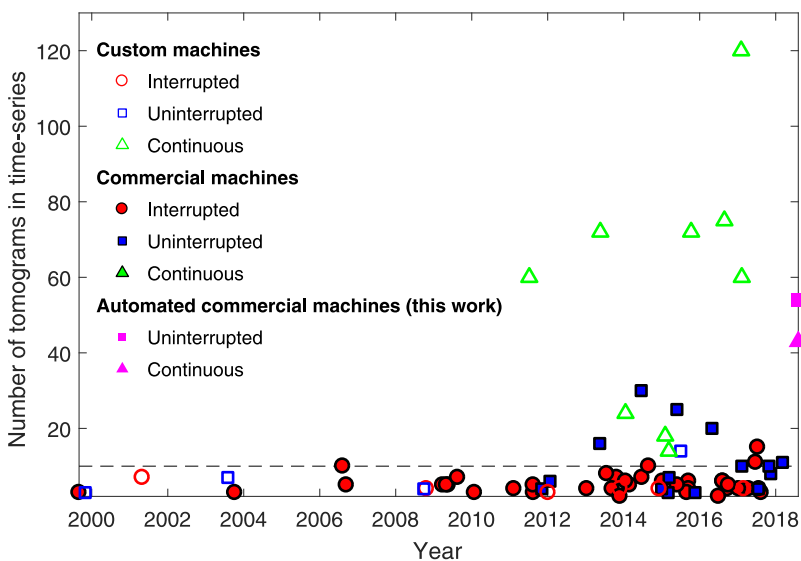

FIG. 2. A summary of previous laboratory-based temporal CT studies, categorised by the temporal CT scanning modes explained in Fig. 1 (interrupted time-lapse, uninterrupted time-lapse, and continuous acquisition), and the machine type (commercial or custom built). The data for this plot are available in Supp. Table I in the supplementary material.

based on *a priori* knowledge of the best acquisition time for an optimal signal to noise ratio. Projections are then acquired in a sequential order as the sample is rotated through a full circle with the angular increment given by dividing 360° by N. However, with this method, any movement is captured progressively over successive projections giving rise to spiral artefacts in the reconstructed tomogram.[25] Furthermore, the same acquisition time must be used throughout and cannot be changed mid-process. One approach to overcome the motion artefacts was to distribute the angles more evenly in time using interlaced sampling.[26] The projections of successive rotations are offset from each other so that they do not overlap, from which subsets are reconstructed with a model-based scheme using prior information. This allowed visualisation of fine dendrites with high spatial and temporal resolution.[27] An alternative approach is a golden-ratio distribution of projection angles that was inspired by the way plants distribute their leaves[28] with the angular increment $\Delta\phi$ equal to the golden ratio times 360°,

$$\Delta\phi = \frac{\sqrt{5}-1}{2} \cdot 360° \approx 222.5°. \tag{1}$$

This approach has the added benefit of allowing the number of projections for each reconstruction to be chosen *ex post facto*. A number of studies have successfully implemented golden-ratio sampling in simulations,[29] in MRI,[30] with neutron tomography,[31,32] and at synchrotron x-ray facilities,[33] but although there is interest for applications on laboratory CT machines, up to now it has not been technically possible.[34]

In this paper, we present two protocols for advanced temporal CT on commercial laboratory systems. The first protocol in Sec. II considers the steps needed to enable automated acquisition of time-lapse CT scans. Interrupted time-lapse is demonstrated through two-way synchronisation with an *in situ* shear cell, whilst the ease of acquiring a large number of uninterrupted scans is demonstrated by collecting 54 tomograms of a slowly germinating mung bean[35] over a 108 h period. Although CT has very recently been used to study seed germination,[36] this is the first high temporally resolved quantification of the process. The second protocol enables continuous streaming with golden-ratio angular sampling. This is the first time golden-ratio sampling of a CT experiment has been used in conjunction with an iterative reconstruction algorithm. The method is applied to analyze mineral precipitation in porous media in Sec. III, allowing a comparison between spatial and temporal resolution of reconstructions with differing numbers of projections. Whilst the protocols may appear similar, they both control the CT system in different ways. The automated time-lapse CT protocol automates the starting of many scans using scan modes already provided on the machine; on the other hand, the continuous golden-ratio acquisition protocol shows how new scan modes can be implemented for temporal CT.

Both protocols were encoded into software extension modules for evaluation on the Nikon High Flux Bay within the Henry Moseley X-ray Imaging Facility (HMXIF), in the Henry Royce Institute at The University of Manchester, UK. The High Flux Bay is a 225 kV walk in room fitted with a

6-axis manipulator and a PerkinElmer 1611 flat panel detector (a size of 4000×4000 pixels and a pixel pitch of 100 μm), running Nikon's proprietary Inspect-X version 5.1.4.3. The software modules were created using the IPC interface[37] to Inspect-X, which allows the proprietary software to be controlled programmatically. The extension modules run alongside Inspect-X, and as the safety interlocks are managed by the proprietary software, the safety of the CT system is unaffected. It should be emphasised that no additional hardware or software modifications were needed for the extension modules to work. The software extension implementations, along with datasets from this paper, can be downloaded from Zenodo.[38]

II. AUTOMATIC TIME-LAPSE CT

There are many situations in which one would like to acquire a series of CT images of objects as they evolve. In the "interrupted" case [Fig. 1(a)], the evolution of the microstructure would be induced by an external influence such as tension,[39] indentation,[40] or electrical charging that can be interrupted.[41] On the other hand, in the "uninterrupted" case [Fig. 1(b)], the sample evolves naturally due to the environment it is placed in, for example, the pupation of a chrysalis[18] or the corrosion of a magnesium alloy.[42] The protocol shown in Fig. 3(a) for acquiring a series of time-lapse scans is similar for both cases with a series of scans each separated by an evolution period. Whilst each step in the protocol is fairly simple, the major obstacle is controlling the x-ray system to perform these tasks without user intervention. Each commercial machine has scan modes that are tailored to the particular instrument, so the first step in a time-lapse protocol is to use these pre-configured modes to start a scan and wait for it to finish. For interrupted time-lapse, it is then necessary to start the forcing mechanism
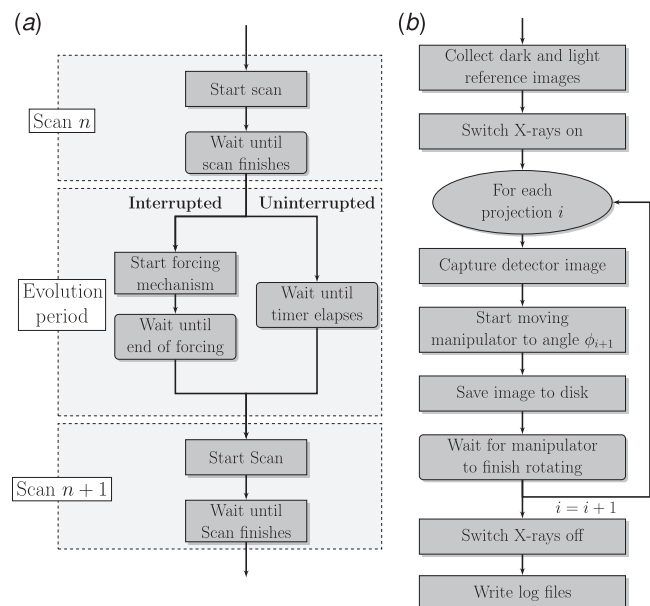

FIG. 3. Protocols for (a) automated time-lapse CT and (b) golden-ratio continuous streaming. Although the steps by themselves appear simple, the challenge is in controlling the x-ray system to automatically perform these operations without user intervention.
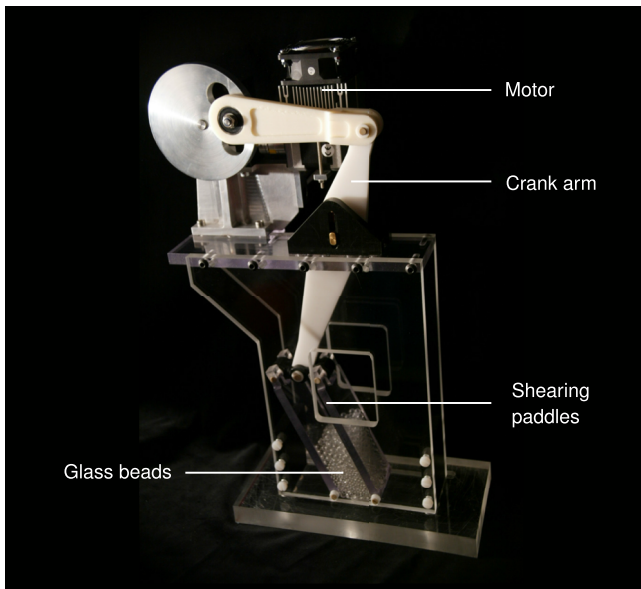
FIG. 4. A shear cell specially developed for studying granular segregation using CT.

and wait for the forcing to finish, with the challenge lying in synchronising the forcing rig with the x-ray system. Although uninterrupted time-lapse simply requires waiting for a timer to elapse, to allow sufficient time for evolution to occur, there are a number of other factors which must be considered. The detector and source performance varies over time, leading to differences of up to 1% in gray scale values in a series of scans performed after several hours interval.[43] This has a significant impact when automatic global gray scale thresholding is used as the sole method of segmenting time-series,[15] and more advanced segmentation techniques are required. Variability in the source can also be mitigated by warming the x-ray beam

during the evolution period whilst waiting for the next scan. Once the evolution period has finished, a subsequent scan must be automatically started.

A. Interrupted time-lapse CT: A synchronised shear cell

We highlight the potential for automated interrupted time-lapse CT by studying granular segregation using a shear cell specially adapted for CT. The shear cell shown in Fig. 4 is of the same dimensions as used previously[44] but with the motors mounted vertically above the unit. This allows the entire cell to rotate within the CT machine without the motors passing through the x-ray beam. A USB (Universal Serial Bus) TTL (transistor-transistor logic) serial cable (FTDI, Glasgow, UK) was used to create two-way communication between the CT acquisition computer and the shear cell. When the x-ray system is ready for the forcing, it sends a TTL pulse to trigger the shear cell, which sends a return pulse back to the acquisition computer when it has finished. The shear cell was initially loaded with a mixture of 6 mm borosilicate glass beads at the bottom and smaller 3 mm beads on the top. The shearing motion forces the mixture of beads to segregate with the smaller beads percolating downwards and the larger beads being squeezed upwards.[45]

The series of CT scans allows the three-dimensional movement of the beads from each shearing motion to be visualised. Figure 5 shows central vertical slices perpendicular to the shearing from two experiments: (a) shows 4 scans with 10 shear cycles between each scan, whilst (b) has 1 shear cycle between each scan. Although the progressive segregation can be appreciated in the former experiment, the large movement of the 6 mm particles between each image means that it is difficult to track the positions of individual spheres from one scan to the next. The segregation is more gradual in the latter experiment, but as the movements
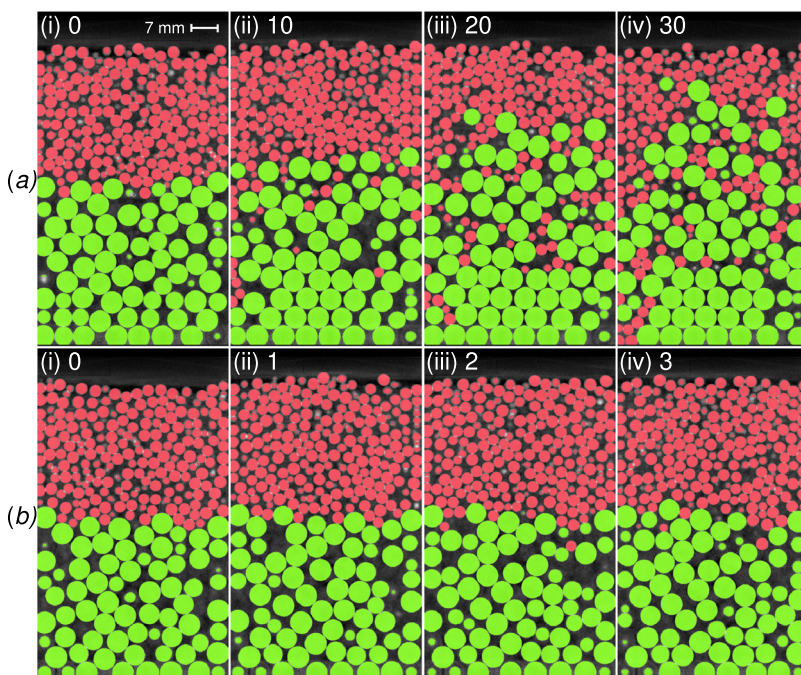

FIG. 5. Segmented and colorised virtual central slices perpendicular to the shearing from two interrupted time-lapse experiments of a granular shear cell filled with 6 mm (colorised green) and 3 mm (red) borosilicate glass beads. (a) comprises of 4 scans with 10 shear cycles between each scan, whilst (b) shows scans separated by 1 shear cycle per scan. The small particles can be seen to percolate downwards, whilst the large particles migrate upwards.

between images are smaller, it is possible to track individual particles.

These preliminary results highlight the importance of evolutionary time scales for time-lapse experiments with the mixing in (b) easily quantifiable. Although it may take hundreds of shear cycles to reach full inversion with the large at the top and small on the bottom,[44] the automatic synchronisation means that it is now possible to have one scan for every shear cycle and further work is currently under way to quantify segregation using CT.

B. Uninterrupted time-lapse CT: Mung bean germination

In order to demonstrate the value of an automated uninterrupted time-lapse approach for collecting many tomograms, we have applied the method to study the germination[36] of a mung bean (*vigna radiata*). These green coloured beans are a vital food crop in Southeast Asia and are often sprouted before eating to improve their nutritional value.[46] Sprouting is the household name for the germination process, during which the bean structure changes significantly as the outer skin (testa) ruptures and the new root (radical) emerges.[47] Although the exact time is sensitive to the surrounding environmental conditions, typically the entire germination process can take the order of a few days, making it a suitable specimen sample for evaluating our method.[35]

1. In vitro method

A sample holder for the bean was created by gluing a piece of 13 mm diameter polyimide tubing to a standard sample mount, as shown in Fig. 6(a). Wet tissue was placed at the bottom of the sample holder, followed by several layers of dry tissue. The bean was placed at the top of the sample holder with small pieces of dry tissue placed around it to secure its position within the tube. The tube was sealed with a cling film to create a moist micro-climate to counter

the drying effect of the warm environment inside the x-ray machine.

An initial dry scan was taken with a similar setup to that described above, except without the wet tissue. The bean was then allowed to imbibe for 3.5 h in ~70° tap-water to initiate the germination process before being carefully transferred back to the sample holder setup for the *in vitro* scans. 54 CT scans were completed during the germination phase at two-hour intervals with the sample remaining inside the machine. All scans comprised of 800 continuously acquired projections with a 708 ms exposure time, 4× binning, 2× frame averaging, a voltage of 65 kV, and a current of 100 μA. The reconstructed voxel size was 18.3 μm^3. Each scan took approximately 18 min with the automatic reconstruction in the proprietary Nikon CT Agent software taking an additional 4 min.

A gray scale slice from the final reconstructed volume of the germination phase is shown in Fig. 6(b). The volumes were processed using TCL scripting in Avizo 9. The raw reconstructed data were first filtered using a 2D non-local means filter. A mask was defined for the region containing tissue paper, and an auto-intensity-thresholded gradient image was subtracted from the entire auto-intensity-thresholded image in this mask region to separate the tissue from the mung bean. The volume of the segmented bean was calculated by performing a label analysis. The poor intensity and textural contrast between the different internal parts of the bean meant that it was impossible to further segment the bean. However, a single slice was manually segmented to highlight the main parts of the bean and is shown in Fig. 6(c).

2. Results

Figure 7 shows 3D volume rendering and 2D slices from different stages of the mung bean germination. Videos of the entire process can be found in the supplementary material (videos S1 and S2). Small tissue artefacts can be seen, but the automated scripting was the most efficient method of segmenting 54 datasets. Qualitatively, it can be seen how the
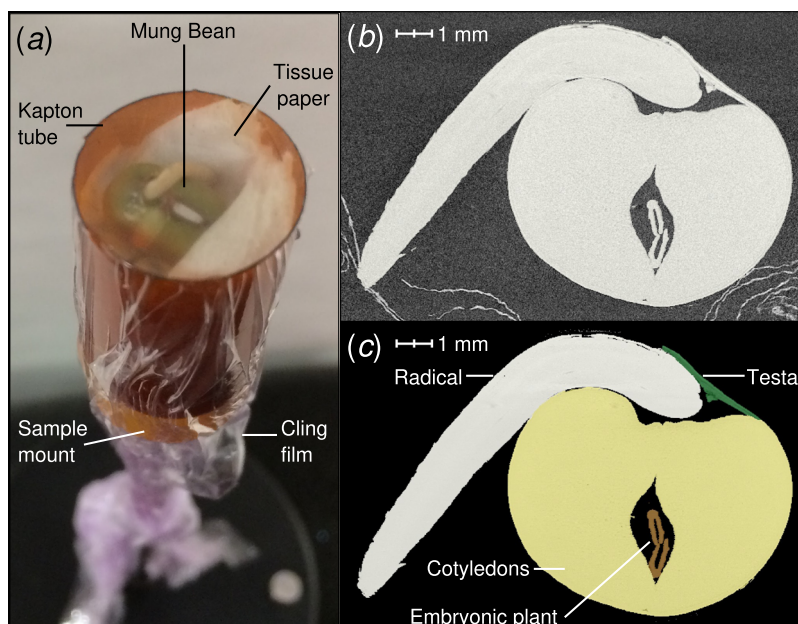

FIG. 6. (a) A photograph of the *in vitro* setup for mung bean germination; (b) a slice of the reconstructed volume showing the gray scale levels; and (c) the same slice colorised using a manual single slice segmentation of the different bean parts. The scale bar is the same size for (b) and (c).
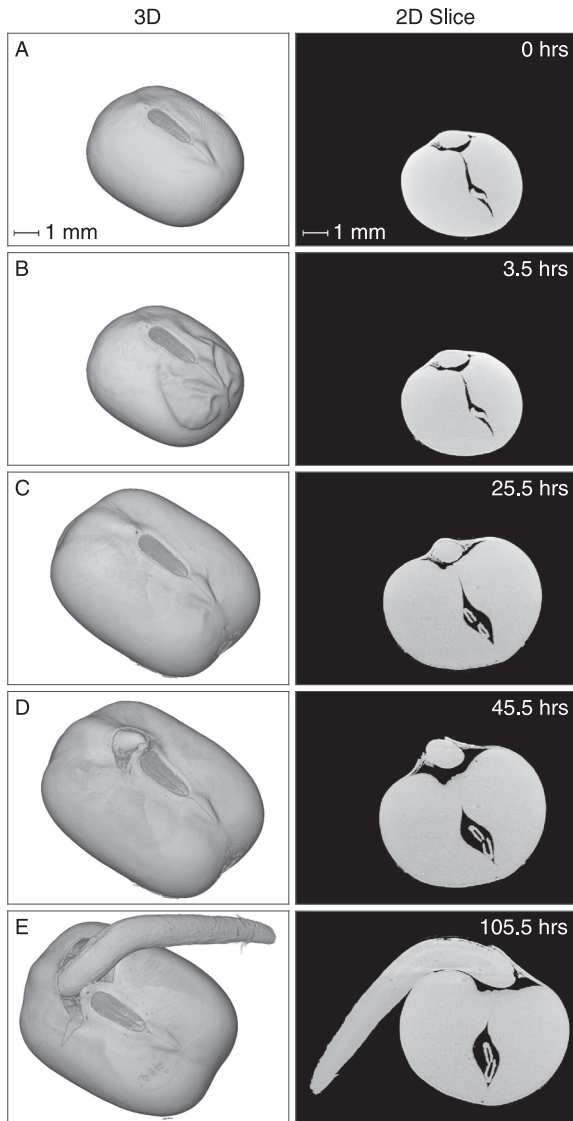
FIG. 7. Stages of mung bean germination captured through micro-XCT with 3D virtual representation and 2D slices shown at different times. The entire evolution can be appreciated in videos S1 and S2 of the supplementary material.

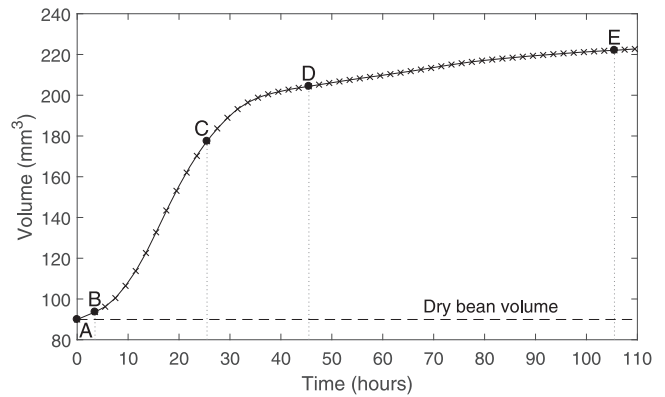
FIG. 8. The 3D volume of the mung bean over time. There are several distinct regimes with labels A-E representing the times shown in Fig. 7.

III. CONTINUOUS GOLDEN-RATIO ACQUISITION: PRECIPITATION OF BARITE

In many practical cases, one is not sure of the optimal scan time in terms of frame rate vs signal-to-noise ratio. In these cases, continuous acquisition with golden-ratio angular sampling provides the flexibility to acquire the data and then decide on the optimal frame rate *ex post facto*.

Here we demonstrate the protocol for continuous golden-ratio acquisition and evaluate its utility as applied to imaging mineral precipitation in porous media. Mineral precipitation is a dynamic process where there is a strong feedback between the reaction kinetics and the reaction products with the varying evolution rates, making it a suitable application for continuous golden-ratio acquisition. The growing crystals progressively clog the pore structure, which reduces ion transport and can limit the precipitation rates.[51] Understanding the evolution of the 3D structure over time is crucial to be able to control and predict the process in nature. This is important to the oil, gas, and hydrothermal energy-recovery industries since fluid circulation through porous rocks can induce precipitation. This in turn causes formation damage, which undermines the efficiency of energy extraction. Additionally, if controlled, precipitation in the subsurface could have important environmental applications, e.g., CO_2 sequestration and to remove radionuclides from contaminated fluids. Barite is an important mineral since it can form during oil extraction due to the mixing of formation waters rich in barium and injected fluids rich in sulphate. It has also been proposed as a barrier for radionuclides in spent nuclear fuel repositories and to remove radionuclides from contaminated flow back water by co-precipitation with barite.

A. Protocol

It was chosen to use golden-ratio sampling[28] of projection angles with the angular increment $\Delta\phi$ given by Eq. (1). If the first projection is at $0°$, then the ith projection angle ϕ_i can be calculated as

$$\phi_i = i \cdot \Delta\phi \quad \mod 360, \tag{2}$$

Compared with the alternative approach of continually making full rotations of $360°$ with a fractional angular increment (see Fig. 9), this golden-ratio strategy has a much larger angular

surface of the bean becomes crinkled after imbibing in water [Fig. 7(b)],[48] before the surface smoothens as the bean expands and swells [Fig. 7(c)]. Finally, the radical emerges [Fig. 7(d)] and elongates [Fig. 7(e)]. Each of these phases can be seen quantitatively in Fig. 8, which shows the evolution of the bean's volume over time. The growth rate is highest between (B) and (C), which corresponds to the swelling of the cotyledons. Between (C) and (D), the growth of the cotyledons slows, but the radical emerges. The slower growth between (D) and (E) is the elongation of the radical. The growth rate of the bean within the system was observed to be qualitatively similar to a control sample subject to the same water and temperature conditions but left outside of the CT system.

The novel use of CT to quantify the germination process also opens doors for using the technique to compare the development of other seeds, for example, the germination of seeds that are genetically modified for harsh climates[49] or the natural adaptation of seeds to unfavorable conditions.[50]
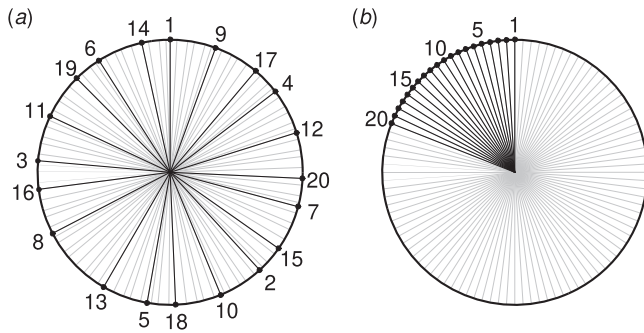
FIG. 9. Schematic showing a comparison between: (a) 100 golden-ratio sampled angular projections given by Eq. (2) and (b) a scan of 100 equi-angular projections. The first 20 projections are labeled and shown in black with the remaining projections shown in gray.
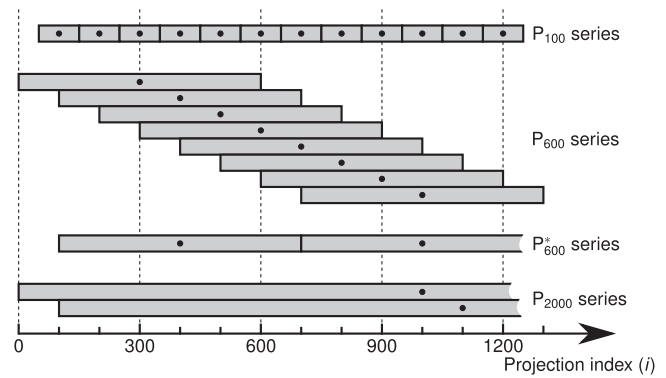

FIG. 10. Schematic showing how different time-series were constructed from subsets of the same continuously acquired projections. The black circles indicate which projection the reconstruction is centered about. See Table I for a summary of the different series.

increment and hence a longer time to move between projections. However, there are a number of advantages. Golden-ratio sampling succeeds in temporally distributing projections more equally across a full circle. As an example, Fig. 9 compares the first 100 golden-ratio sampled projections with a scan of 100 equi-angular projections (spaced by an angular increment of $3.6°$). The first 20 golden-ratio projections have already completed 7 full rotations, whilst 20 equi-angular projections have only covered $72°$. As golden-ratio sampling continuously covers a circle every 3 projections, the acquisition can be stopped at any point and a reasonable reconstruction may still be achieved with a quality that depends solely on the total number of projections used to reconstruct. In a certain sense, golden-ratio angular sampling is optimal[52] with each projection containing information about the object as independent from previous projections as possible. It is also noteworthy that as the golden ratio is irrational, each projection angle is unique and never re-sampled even if tens of thousands of projections are acquired.

The basic protocol for golden-ratio continuous sampling is shown in Fig. 3(b). Given the longer time to move the manipulator, the image save can be moved to occur in parallel with the manipulator rotation. Whilst the protocol appears to be a trivial set of operations, the greatest challenge for commercial machines is gaining access to the x-ray source, manipulator, and imaging sub-systems to implement each step. An extension module was successfully coded for Nikon machines that is available for download.[38]

B. Experimental acquisition

A column of sintered glass beads approximately 10 mm long and 6 mm in diameter was vertically constricted by heat shrink tube and connected to a flow rig developed at HMXIF. Solutions of barium chloride (1 mmol $BaCl_2$) and sodium sulphate (1 mmol Na_2SO_4) were delivered at a constant flow rate of 0.34 ml min^{-1} using high pressure ISCO syringe pumps. The fluids have a mixing time of approximately 1.8 min before entering the sample, which is expected to be sufficient to induce significant crystal nucleation.[53]

An initial dry scan was performed using the proprietary Inspect-X circular scan mode with 3141 projections acquired at a voltage of 120 kV, a current of 67 μA, 2× binning, 4× frame averaging, and an exposure time of 1.4 s. After completion of the dry scan, the flow was started and the software extension was used to continuously acquire 4400 projections over 11 h with the same imaging conditions as the dry scan, except 1× frame averaging. Each projection took an average of 8.9 s to acquire, with ~3.5 s to clear the detector buffer and capture the new image and ~5.4 s to move the manipulator. In other words, 60% of the time for each projection was needed to move the manipulator, whilst 40% was needed for acquiring the image. The final projections were 2000 × 2000 pixels in size. The source-to-center and source-to-detector distances were 30.2 mm and 1404.0 mm, respectively, giving a final reconstructed voxel size of 4.3 μm^3.

To investigate the spatial-temporal resolution trade-off, three time series of reconstructions P_{100}, P_{600}, and P_{2000} were computed using 100, 600, and 2000 projection subsets, respectively, as shown in Fig. 10. The individual reconstructions in each time series are centered about a projection index i, indicated by a superscript, and spaced apart by 100 projections. For example, the first reconstruction in the P_{100} series is $P_{100}^{(100)}$, which is centered about projection 100 and uses projections 51-150 for the reconstruction, whilst the second member of the series is $P_{100}^{(200)}$. The series are summarised in Table I. The projections used in one P_{100} reconstruction do not overlap with those used in the previous or next reconstruction. However, the P_{600} series implies an overlap of 500 projections used between consecutive reconstructions. For instance, $P_{600}^{(300)}$ uses projections 1-600 and $P_{600}^{(400)}$ uses projections 101-700 with projections 101-600 common to both. As a comparison, a subset of P_{600} known as P_{600}^* with reconstructions using

TABLE I. A summary of the different reconstruction time-series.

Series	Interval	Min index	Max index	Reconstructions in series
P_{100}	100	100	4200	$P_{100}^{(100)}, P_{100}^{(200)}, \ldots, P_{100}^{(4200)}$
P_{600}	100	300	4000	$P_{600}^{(300)}, P_{600}^{(400)}, \ldots, P_{600}^{(4000)}$
P_{600}^*	600	400	4000	$P_{600}^{(400)}, P_{600}^{(1000)}, \ldots, P_{600}^{(4000)}$
P_{2000}	100	1000	3300	$P_{2000}^{(1000)}, P_{1000}^{(1100)}, \ldots, P_{2000}^{(3300)}$

non-overlapping projections (i.e., an interval of 600) was also used for quantitative analysis in Fig. 14. The golden-ratio angular sampling scheme allows this way of increasing the temporal resolution from a single time lapse dataset; however, care must be taken to interpret the results as projections are reused for different reconstructions. In practice, this means that any difference between consecutive reconstructions is due to changes in the sample within the non-overlapping 100 projections.

The native Nikon CT Pro reconstruction software uses an equi-angular FDK (Feldkamp, Davis, and Kress[54]) implementation and performs many operations such as alignment automatically. Although the golden-ratio subsets are not equi-angular, after reordering subsets of projections in ascending angular order and manually applying shading corrections, the CT Pro software can be used to obtain approximate reconstructions. An in-house reconstruction scheme was also constructed using a MATLAB implementation[55] of the iterative Conjugate Gradient Least Squares (CGLS) algorithm.[56] The ASTRA Tomography Toolbox[57,58] was used to employ GPU-acceleration of the computationally most expensive steps of forward- and back-projection. 50 iterations of the CGLS algorithm were empirically found to provide the optimal trade-off between resolution and noise and were used in all cases. Prior to reconstruction, the individual projection images were subjected to global horizontal centering and rotation-stage tilt corrections with the parameters determined from the reconstruction of the static dry scan using the proprietary Nikon CT Pro software. An additional individual horizontal alignment of projections using the sharp edge of the flow cell was found to improve reconstruction quality. The need for this correction is believed to originate from the slight sample movement due to the fast rotation of the rigid tubing connected to the flow cell.

C. Results

Single reconstructions $P_{100}^{(1000)}$, $P_{600}^{(1000)}$, and $P_{2000}^{(1000)}$ were performed using both the proprietary FDK and the iterative CGLS methods with Fig. 11 showing 2.15 mm × 2.15 mm regions of interest (ROI). With as few as 100 projections, the FDK reconstruction produces a significant amount of speckled noise that is difficult to distinguish from the crystals and certainly could not be accurately segmented. The CGLS reconstruction for $P_{100}^{(1000)}$ is markedly clearer with the crystals identifiable from beads and pore spaces. FDK performance improves with more projections; however, upon close examination, the iterative reconstructions still produce sharper crystal boundaries. With significantly better performance for P_{100}, the iterative CGLS scheme was chosen to reconstruct the entire time-series and perform analyses in the remainder of this paper.

Comparing the P_{100}, P_{600}, and P_{2000} series, it can be seen that a larger number of projections give sharper boundaries between the individual crystals. Distinguishing the interfaces is important for an accurate quantification of the volume and surface area of crystals. For example, the noise and low spatial resolution for $P_{100}^{(1000)}$ blurs the space between crystals, making them undistinguishable (also see video S3 of the
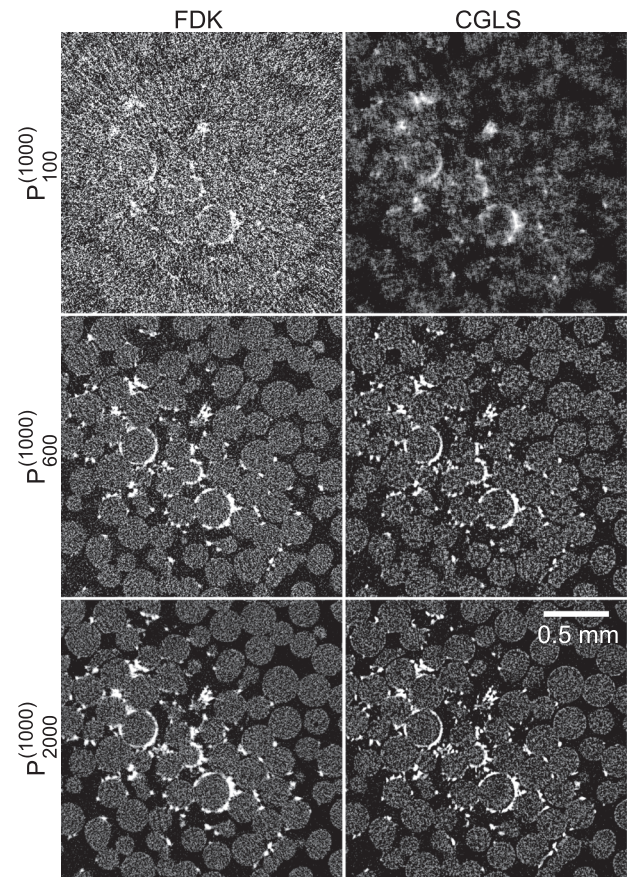

FIG. 11. Comparisons of reconstructions using FDK performed using Nikon's proprietary CTPro and a custom reconstruction implementing the iterative CGLS algorithm. Gray scale regions of interest of size 2.15 mm × 2.15 mm from the same horizontal slice are shown for reconstructions $P_{100}^{(1000)}$, $P_{600}^{(1000)}$, and $P_{2000}^{(1000)}$. Barite is white, glass beads are light gray, and fluid (pores) is dark gray.

supplementary material). As the barite has a highly contrasting gray scale level, the blurring would likely lead to an overestimation of the total volume and possibly an underestimation of the surface area. We also note that crystal boundaries are sharper for $P_{2000}^{(1000)}$ than for $P_{600}^{(1000)}$. Although this is expected for a static scan, it is seemingly counter-intuitive for a temporally evolving sample since the movement and growth of crystals over the 4.9 h needed to acquire 2000 projections would be expected to blur the crystal boundaries. This blurring would also be expected to be most significant for $P_{2000}^{(1000)}$ since it corresponds to the first 4.9 h of the experiment when the crystal growth rate is highest. However, Fig. 11 shows surprisingly sharp interfaces of glass beads and crystals, which is possibly due to slowing reaction rates over time with most crystals nucleating within the earliest 1000 projections. A second interesting observation is that the number of crystals in $P_{100}^{(1000)}$ is lower than for $P_{600}^{(1000)}$ and $P_{2000}^{(1000)}$. The higher number of crystals present for larger numbers of projections is a consequence of low temporal resolution. That is, the projections used in P_{600} cover longer periods of time during which more crystals have nucleated in the pore structure than in P_{100}. In the same manner, P_{2000} shows even more crystals than P_{600}. Consequently, during the initial growth period when the number of crystals
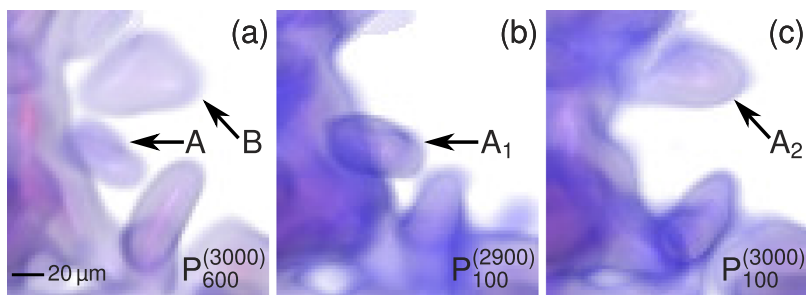
FIG. 12. Doubling of crystals can be found for higher numbers of projections in the reconstruction due to poor temporal resolution. The seemingly two crystals A and B seen in the 3D visualisation of $P_{600}^{(3000)}$ (a) are in fact one single crystal in the P_{100} series with the crystal in position A_1 for $P_{100}^{(2900)}$ (b) but in position A_2 in $P_{100}^{(3000)}$ (c).

invading the pore structure is larger, the poor temporal resolution of P_{600} and P_{2000} would result in the over-estimation of the total volume of crystals.

Although the crystal boundaries for P_{600} and P_{2000} appear to show increasing clarity, the movement and growth of crystals over the 1.5 and 4.9 h necessary to acquire 600 and 2000 projections can lead to artefacts. Figure 12(a) seemingly shows two crystals A and B for $P_{600}^{(3000)}$; however, by comparing with the same spatial position in P_{100} at consecutive time steps [Figs. 12(b) and 12(c)], we can see that it is in fact one crystal that has suddenly moved from position A_1 to A_2. Although the crystal is in different positions for the $P_{100}^{(2900)}$ and $P_{100}^{(3000)}$ reconstructions, projections containing the crystal in both spatial positions are used for $P_{600}^{(3000)}$ and $P_{2000}^{(3000)}$, causing the doubling artefact. If instead of a sudden change of position the crystal continuously moved between positions A_1 and A_2, the effect would be the formation of a header and tail that makes the crystal artificially elongated in the moving direction. Both cases lead to an overestimation of the crystal volume and also the surface area. In our experiment, most crystals settle over time as the pore structure clogs; thus, the overestimation of crystals

is only temporary (videos S4, S6, and S8) and is expected to be progressively less important over time.

Figure 13 shows the precipitation of barite (white crystals) over time for P_{600}. Similar time-series for P_{100} and P_{2000} can be found in the supplementary material. In general, the number of crystals is higher closer to the inlet (bottom of the picture) and decreases further upwards in the column. This is expected due to the high saturation index used here that has been shown to cause nucleation in the fluid.[53] These crystals can be transported in the flow stream and eventually be deposited on the glass surfaces. The deposition of crystals seems to take place where faster flow is expected: First, at the center of the column, and then once the main flow paths at the center are clogged, accumulation is seen closer to the inlet and spread throughout the diameter of the column. Crystals are expected to get trapped by a filtration mechanism as they grow and are transported through the permeable flow paths.

From video S5 (see the online supplementary material), barite crystals can be observed in the pores in the first reconstruction, $P_{600}^{(300)}$ reconstruction. In the P_{100} series (video S3),
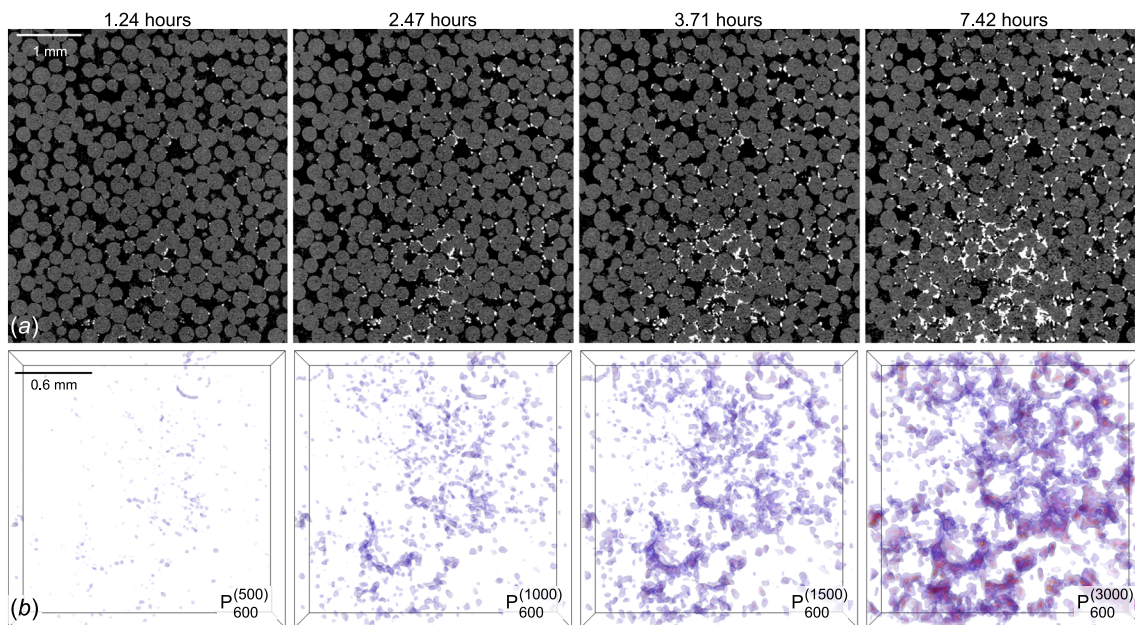

FIG. 13. (a) Gray scale slices parallel to the flow direction (of size 4.3 mm × 4.8 mm) and (b) 3D visualisations (of sub-volumes 2.15 mm × 1.72 mm × 1.72 mm at the center bottom of the sample) from the P_{600} series. In (a), the white corresponds to barite, the light gray corresponds to glass, and dark gray corresponds to fluid (pores). In (b), the pores and glass are set to transparent and only the crystals are rendered. The colour scheme relates to the absorption of crystals where hotter (more red) colours correspond to denser voxels, and more blue colours correspond to less dense voxels. Videos showing the full temporal evolution can be found in the online supplementary material, along with corresponding videos for P_{100} and P_{2000}.

crystals can be visually identified first in $P_{100}^{(300)}$. Nevertheless, it was not possible to quantify the volume of crystals before $P_{100}^{(400)}$ since in $P_{100}^{(300)}$, crystals could not be distinguished from noise by thresholding the pixel intensity. This allows for an interesting analysis of the method's efficiency to capture the early stages of growth.

When the size of crystals are below what can be resolved before projections 300-400, it is expected that the first reconstruction $P_{600}^{(300)}$ would show only very faint crystals (as they appear only on the second half of the projection set). Contrarily for P_{100}, crystals are present, for example, between projections 451 and 550. Therefore, it is expected that the higher temporal resolution of P_{100} would yield a more resolved reconstructed dataset for more accurate quantification at least up to projection 700. This is when P_{600} can be used without the overlap of projections that we know do not contain spatially resolvable crystals.

Bearing in mind the spatial and temporal artefacts discussed above, it is clear that the number of projections can have an important impact on the quantification of crystal growth over time. Figure 14(a) shows that the volume of crystals measured from a different number of projections can differ up to a factor of 3. During the initial 1000 projections, the volume is smaller when fewer projections are used in the reconstruction. Although it was predicted from the observations that P_{600} and P_{2000} would overestimate the volume of crystals at early time due to low temporal resolution, this is only true for P_{2000} with P_{100} and P_{600} showing similar values. After 1000 projections, the volume from P_{100} increases at a faster rate than P_{600} and P_{2000}. This is possible evidence of the volume overestimation, arising from the space between neighbour crystals appearing as crystal due to the poor spatial resolution.

The growth rate at the $i + 1$th projection was calculated as[53]

$$R_{i+1} = \frac{\Delta V}{V_m \Delta t} \frac{2}{A_i + A_{i+1}}, \quad (3)$$

with ΔV being the change in crystal volume, Δt being the change in time, V_m being the ratio of the molecular weight (233.4 g mol^{-1}) to the density (4.48 g cm^{-3}), and the second fraction representing the average total surface area of crystals over the time period. Interestingly, the growth rate shown in Fig. 14(b) does not follow the same trends observed for the volume in Fig. 14(a), implying that the spatial-temporal artefacts discussed above have different effects on the volume and surface area over time and should be further investigated beyond this paper. The rates calculated from P_{2000} and P_{600}^* are similar and do not allow to draw any information from the beginning of the experiment. P_{100} and P_{600} show an accentuated decrease in the growth rate during the first 3 h of the experiment, which is a consequence of reduced fluid mobility through some flow paths.[5,59] We note that the rates calculated from P_{100} are faster than from P_{600}, but that there is a higher variability of the rate trend corresponding to P_{100}. However, these faster rates for P_{100} compared to P_{600} are difficult to explain based on the divergent increase in the crystal volume shown in Fig. 14(a). This behavior could be related from the dense barite crystal observed for P_{100}. These artefacts lead to an over-estimation of the volume and have unpredictable effects on the surface area. Since the amount and type of each artefact vary with time, and since their effects on volume are not proportional to their effects on the surface area, the differences in growth rate for the different reconstruction methods are attributed to the artefacts inherent to temporal CT.

D. Conclusion

In conclusion, by using continuous golden-ratio acquisition coupled with an iterative reconstruction scheme to visualise mineral precipitation, we have been able to analyze spatial and temporal effects using 100, 600, and 2000 projections in the reconstruction. We identify two main sources of error: (1) blurring of crystals for P_{100} due to lower spatial resolution and (2) doubling of crystals for P_{600} and P_{2000} due to lower temporal resolution. In an ideal situation, it would be preferable to use 600 or more projections but with a higher temporal resolution. Currently the time taken to move the manipulator through $\Delta\phi$ (1) is 5.4 s, which is 60% of the total time for each projection. By contrast, the same CT machine with the same exposure time takes 1.9 s to move through 3.6° (for an equi-angular scan with 100 projections), which is 35% of the total projection time. Hence, one method for reducing the movement time, and hence increasing the temporal frequency, would be to decrease the magnitude of $\Delta\phi$. Smaller irrational angular increments such as $\Delta\phi/7$ or $\Delta\phi/11$ could be tested for improved performance.

One clear advantage of the golden-ratio scheme was that reconstructions can be performed from the same dataset with any number of projections. With traditional circular scanning, this optimization would require multiple experiments with varying temporal and spatial resolution. With growth rates changing during an experiment, golden-ratio scanning also
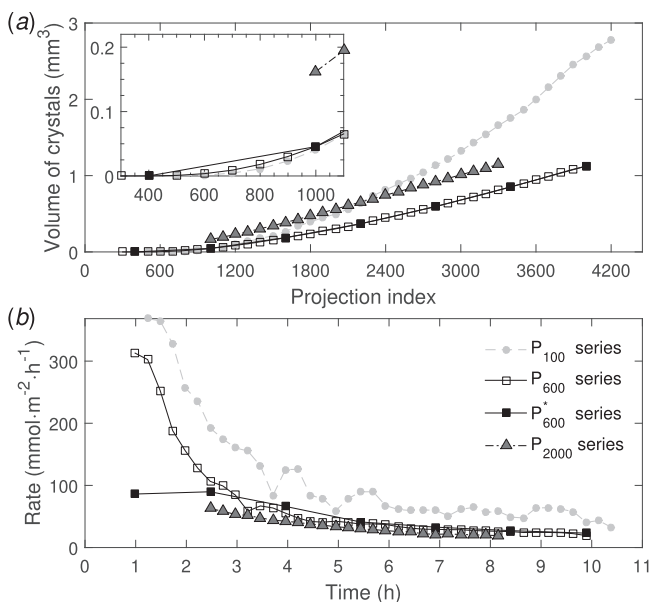
FIG. 14. Quantification of (a) the total volume of crystals and (b) the overall crystal growth rate calculated from Eq. (3) for each of the reconstruction modes shown in Fig. 10 and Table I. The inset in (a) highlights the volume variation over the initial 1100 projections. Note that the x-scale for both graphs is the same with the projection index labeled in (a) and the time since the start of the experiment in (b).

allows different numbers of projections to be used at different points in the experiment. Thus the present work can be seen as a step toward "smart" reconstruction methods that adapt to features found in the sample.

We emphasise that CGLS was used in the present work as a simple example of an iterative reconstruction method providing advantages over FDK. In recent years, a substantial amount of work has been devoted to developing new reconstruction algorithms to compensate for incomplete data such as few projections or a limited angular range. Notably, sparsity[60–62] and spatio-temporal[63,64] regularisation methods have been employed with great success to improve reconstruction quality in case of few projections. More work is needed to advance such methods for routine use, including addressing questions of how few projections suffice[65,66] to provide accurate reconstructions for different types of samples. This, however, is much beyond the scope of the present work for which the focus was to demonstrate the capability for enabling temporal CT on existing laboratory CT instruments.

The continuous golden-ratio acquisition extension would be useful not only to scan other laboratory setups involving flow cells[19] but also to study other chemical processes where the kinetics change during the course of a reaction.

IV. DISCUSSION AND FURTHER SCOPE

In this paper, we have advanced the automated temporal CT capabilities of laboratory CT machines by implementing generic protocols for: (1) Automated time-lapse CT and (2) a continuous golden-ratio acquisition. These protocols overcome the restrictions placed on laboratory machines by proprietary manufacturers' software, and three real applications were presented.

The generic protocol for time-lapse CT was presented in Sec. II with implementations of both the interrupted and uninterrupted cases. The ability to automatically synchronise a commercial system with an *in situ* rig was highlighted with a shear cell used to study granular segregation. Automatic synchronisation of *in situ* rigs would be an invaluable development for other laboratory time-lapse studies such as the compression of foams and other materials[67,68] or the charging of batteries[69] and would also be particularly advantageous for laboratory Digital Volume Correlation (DVC) studies.[70] The capability of automated uninterrupted time-lapse with large numbers of tomograms was demonstrated through the first use of CT to examine the uninterrupted germination of a mung bean with 54 scans performed over a 108 h period. This certainly opens up the possibility of acquiring many datasets of evolving processes in the labs and could be used to build uninterrupted temporal pictures of salt evaporation, fungal decay, the drying of plaster, or even battery degradation.

In Sec. III, we present the first laboratory application of continuous projection acquisition with golden-ratio angular sampling. An initial comparison showed how an iterative reconstruction scheme gave significant improvements in image quality over the standard FDK algorithm usually used in commercial software, with more resolved boundaries especially for lower numbers of projections. Using the iterative scheme, we created different time series using subsets of 100, 600, and 2000 projections in each reconstruction; in doing so, we were able to examine the spatial and temporal effects of different numbers of projections in a reconstruction. Although the crystals were constantly changing, the reconstructions with 2000 projections were surprisingly sharp as a result of the golden-ratio scheme giving an equal temporal distribution of projections around a circle.[25] However, whilst higher numbers of projections gave spatially sharper images, they caused doubling of crystals that moved during the time required to acquire those projections. Lower numbers of projections have reduced spatial resolution that blurs crystal boundaries although the temporal resolution is higher. Further work must be done to quantify these spatial and temporal artefacts, whilst the sampling method should also be optimised to increase the temporal acquisition rate. A wider availability of iterative reconstruction schemes on commercial machines would also aid their usefulness for time-based studies with high temporal resolution.

Clearly, these protocols by themselves unlock the temporal capabilities of commercially available laboratory CT machines. Whilst the particular software modules have been implemented on CT systems running Nikon's Inspect-X, the general protocols could be ported to other commercially available machines, provided that software libraries are supplied for programmatic control of the systems. Similar approaches may also be possible for other laboratory-based tomography systems, for example, gamma-tomography.[71] Moreover, from a wider perspective, this paper serves to highlight the wide flexibility of laboratory machines when they can be custom controlled. It opens up the possibility of using laboratory machines to generate customised datasets for new reconstruction algorithms. As a first example, the golden-ratio dataset from this paper could be used to test algorithms for both local and global temporal smoothing.[72] Other temporal schemes that give higher spatial resolution than golden angle sampling such as "Time-interlaced model-based iterative reconstruction" (TIMBIR)[26] can also now be adapted for laboratory machines. Acquisition could also be performed from noncustom geometries such as a tilted rotate-axis of the manipulator, opening the potential of standard CT machines to perform laminography.[73]

SUPPLEMENTARY MATERIAL

Please see the online supplementary material for the following videos associated with this paper:

S1. 3D visualisation of mung bean (*vigna radiata*) germination;

S2. 2D slice through a germinating mung bean (*vigna radiata*);

S3. 2D gray scale slice of barite precipitation in porous media using P_{100};

S4. 3D visualisation of barite precipitation in porous media using P_{100};

S5. 2D gray scale slice of barite precipitation in porous media using P_{600};

S6.   3D visualisation of barite precipitation in porous media using P_{600};
S7.   2D gray scale slice of barite precipitation in porous media using P_{2000};
S8.   3D visualisation of barite precipitation in porous media using P_{2000}.

In addition, the data for reproducing Fig. 2 are also provided in supplementary material Table I.

ACKNOWLEDGMENTS

[1] S. R. Stock, Int. Mater. Rev. **53**, 129 (2008).
[2] L. Schoeman, P. Williams, A. du Plessis, and M. Manley, Trends Food Sci. Technol. **47**, 10 (2016).
[3] R. Mizutani and Y. Suzuki, Micron **43**, 104 (2012).
[4] V. Cnudde and M. N. Boone, Earth-Sci. Rev. **123**, 1 (2013).
[5] J. R. A. Godinho and P. J. Withers, Geochim. Cosmochim. Acta **222**, 156 (2018).
[6] J. Kastner, Case Stud. Nondestr. Test. Eval. **6**, 2 (2016), special issue: Industrial computed tomography.
[7] P. J. Withers and P. D. Lee, Ingenia **51**, 40 (2012).
[8] A. du Plessis, S. G. le Roux, J. Els, G. Booysen, and D. C. Blaine, Case Stud. Nondestr. Test. Eval. **4**, 1 (2015).
[9] S. A. McDonald and P. J. Withers, J. Strain Anal. Eng. Des. **49**, 257 (2014).
[10] H. A. Bale, A. Haboub, A. A. MacDowell, J. R. Nasiatka, D. Y. Parkinson, B. N. Cox, D. B. Marshall, and R. O. Ritchie, Nat. Mater. **12**, 40 (2012).
[11] P. H. Kamm, F. García-Moreno, T. R. Neu, K. Heim, R. Mokso, and J. Banhart, Adv. Eng. Mater. **19**, 1600550 (2017).
[12] T. De Kock, M. Boone, T. De Schryver, J. Van Stappen, H. Derluyn, B. Masschaele, G. De Schutter, and V. Cnudde, Environ. Sci. Technol. **49**, 2867 (2015).
[13] E. Maire, C. Le Bourlot, J. Adrien, A. Mortensen, and R. Mokso, Int. J. Fract. **200**, 3 (2016).
[14] W. M. Thompson, W. R. B. Lionheart, E. J. Morton, M. Cunningham, and R. D. Luggar, Meas. Sci. Technol. **26**, 055401 (2015).
[15] E. Maire and P. J. Withers, Int. Mater. Rev. **59**, 1 (2014).
[16] S. C. Garcea, Y. Wang, and P. J. Withers, Compos. Sci. Technol. **156**, 305 (2018).
[17] J. Y. Buffiére, E. Maire, J. Adrien, J. P. Masse, and E. Boller, Exp. Mech. **50**, 289 (2010).
[18] T. Lowe, R. J. Garwood, T. J. Simonsen, R. S. Bradley, and P. J. Withers, J. R. Soc., Interface **10**, 20130304 (2013).
[19] T. Bultreys, M. A. Boone, M. N. Boone, T. D. Schryver, B. Masschaele, L. V. Hoorebeke, and V. Cnudde, Adv. Water Resour. **95**, 341 (2016).
[20] S. Ahmed, T. N. Klassen, S. Keyes, M. Daly, D. L. Jones, M. Mavrogordato, I. Sinclair, and T. Roose, Plant Soil **401**, 125 (2016).
[21] S. Raneri, V. Cnudde, T. De Kock, H. Derluyn, G. Barone, and P. Mazzoleni, Eur. J. Mineral. **27**, 279 (2015).
[22] M. Dierick, D. V. Loo, B. Masschaele, J. V. den Bulcke, J. V. Acker, V. Cnudde, and L. V. Hoorebeke, in *1st International Conference on Tomography of Materials and Structures* [Nucl. Instrum. Methods Phys. Res., Sect. **324**, 35 (2014)].
[23] G. R. Myers, A. M. Kingston, T. K. Varslot, M. L. Turner, and A. P. Sheppard, Appl. Opt. **50**, 3685 (2011).
[24] D. Vavřík, J. Jakůbek, I. Kumpova, and M. Pichotka, J. Instrum. **12**, C02010 (2017).
[25] A. P. Kaestner, B. Munch, P. Trtik, and L. Butler, Opt. Eng. **50**, 123201 (2011).
[26] K. A. Mohan, S. V. Venkatakrishnan, J. W. Gibbs, E. B. Gulsoy, X. Xiao, M. D. Graef, P. W. Voorhees, and C. A. Bouman, IEEE Trans. Comput. Imaging **1**, 96 (2015).
[27] J. W. Gibbs, K. A. Mohan, E. B. Gulsoy, A. J. Shahani, X. Xiao, C. A. Bouman, M. De Graef, and P. W. Voorhees, Sci. Rep. **5**, 11824 (2015).
[28] T. Kohler, in *IEEE Symposium Conference Record Nuclear Science* 2004 (IEEE, 2004), Vol. 6, pp. 3961–3965.
[29] H. Wang, A. Kaestner, Y. Zou, Y. Lu, and Z. Guo, in *Neutron Imaging for Applications in Industry and Science Proceedings of the 8th International Topical Meeting on Neutron Radiography (ITMNR-8) Beijing, China, 4–8 September* 2016 [Phys. Procedia **88**, 290 (2017)].
[30] S. Winkelmann, T. Schaeffter, T. Koehler, H. Eggers, and O. Doessel, IEEE Trans. Med. Imaging **26**, 68 (2007).
[31] L. G. Butler, B. Schillinger, K. Ham, T. A. Dobbins, P. Liu, and J. J. Vajo, in *Proceeding of the Ninth World Conference on Neutron Radiography ("The Big-5 on Neutron Radiography")* [Nucl. Instrum. Methods Phys. Res., Sect. A **651**, 320 (2011)].
[32] A. P. Kaestner, P. Trtik, M. Zarebanadkouki, D. Kazantsev, M. Snehota, K. J. Dobson, and E. H. Lehmann, Solid Earth **7**, 1281 (2016).
[33] K. Ham, H. A. Barnett, T. Ogunbakin, D. G. Homberger, H. H. Bragulla, K. L. Matthews, C. S. Willson, and L. G. Butler, Proc. SPIE **6318**, 631822 (2006).
[34] J. Adrien, S. Meille, S. Tadier, E. Maire, and L. Sasaki, Cem. Concr. Res. **82**, 107 (2016).
[35] E. Seccombe, "Grow: Experiencing nature in the fifth dimension," Ph.D. thesis, School of Art and Design, The Australian National University, 2016.
[36] S. Blunk, A. H. Malik, M. I. de Heer, T. Ekblad, K. Fredlund, S. J. Mooney, and C. J. Sturrock, Biomed. Phys. Eng. Express **3**, 044001 (2017).
[37] P. Gajjar, "IPC quick start guide," Technical Report No. XTM0499-A1, The University of Manchester and Nikon Metrology, Tring, HP23 4JX, UK, 2017.
[38] P. Gajjar *et al.* (2018). "New software protocols for enabling laboratory based temporal CT," Zenodo, https://doi.org/10.5281/zenodo.1204088.
[39] F. Pierron, S. A. McDonald, D. Hollis, J. Fu, P. J. Withers, and A. Alderson, Strain **49**, 467 (2013).
[40] A. Bouterf, S. Roux, F. Hild, J. Adrien, E. Maire, and S. Meille, Strain **50**, 444 (2014).
[41] D. S. Eastwood, V. Yufit, J. Gelb, A. Gu, R. S. Bradley, S. J. Harris, D. J. L. Brett, N. P. Brandon, P. D. Lee, P. J. Withers, and P. R. Shearing, Adv. Energy Mater. **4**, 1300506 (2014).
[42] H. M. Krebs, A. Chirazi, L. Lechner, J. Gelb, X. Zhou, G. E. Thompson, and P. J. Withers, in *Frontiers in Materials Processing, Applications, Research and Technology*, edited by M. Muruganant, A. Chirazi, and B. Raj (Springer, Singapore, 2018), pp. 165–177.
[43] T. Lowe, "Time dependent variations in x-ray computed tomography data during repeated scanning," Technical Report, The University of Manchester, 2016.
[44] K. van der Vaart, P. Gajjar, G. Epely-Chauvin, N. Andreini, J. M. N. T. Gray, and C. Ancey, Phys. Rev. Lett. **114**, 238001 (2015).
[45] P. Gajjar, K. van der Vaart, A. R. Thornton, C. G. Johnson, C. Ancey, and J. M. N. T. Gray, J. Fluid Mech. **794**, 460 (2016).
[46] T. A. El-Adawy, E. H. Rahma, A. A. El-Bedawey, and A. E. El-Beltagy, Plant Foods Hum. Nutr. **58**, 1 (2003).
[47] J. D. Bewley, K. J. Bradford, H. W. M. Hilhorst, and H. Nonogaki, *Seeds*, 3rd ed. (Springer, New York, NY, 2013).
[48] K. Kikuchi, M. Koizumi, N. Ishida, and H. Kano, Ann. Bot. **98**, 545 (2006).
[49] D. López-Arredondo, S. I. González-Morales, E. Bello-Bello, G. Alejo-Jacuinde, and L. Herrera, F1000Research **4**, 651 (2015).
[50] I. Baxter, J. N. Brazelton, D. Yu, Y. S. Huang, B. Lahner, E. Yakubova, Y. Li, J. Bergelson, J. O. Borevitz, M. Nordborg, O. Vitek, and D. E. Salt, PLoS Genet. **6**, e1001193 (2010).
[51] J. R. A. Godinho, K. Chellappah, I. Collins, P. Ng, M. Smith, and P. J. Withers, "Time-lapse imaging of particle invasion and deposition in porous media using in situ X-ray radiography," J. Pet. Sci. Eng. (unpublished).
[52] I. G. Kazantsev, S. Matej, and R. M. Lewitt, in *Proceedings of the Workshop on Discrete Tomography and its Applications* [Electron. Notes Discrete Math. **20**, 205 (2005)].
[53] J. R. A. Godinho and A. G. Stack, Cryst. Growth Des. **15**, 2064 (2015).

[54] L. A. Feldkamp, L. C. Davis, and J. W. Kress, J. Opt. Soc. Am. A **1**, 612 (1984).

[55] P. C. Hansen, Numer. Algorithms **46**, 189 (2007).

[56] M. R. Hestenes and E. Stiefel, J. Res. Natl. Bur. Stand. **49**, 409 (1952).

[57] W. van Aarle, W. J. Palenstijn, J. De Beenhouwer, T. Altantzis, S. Bals, K. J. Batenburg, and J. Sijbers, Ultramicroscopy **157**, 35 (2015).

[58] W. van Aarle, W. J. Palenstijn, J. Cant, E. Janssens, F. Bleichrodt, A. Dabravolski, J. De Beenhouwer, K. J. Batenburg, and J. Sijbers, Opt. Express **24**, 25129 (2016).

[59] J. R. A. Godinho, K. M. Gerke, A. G. Stack, and P. D. Lee, Sci. Rep. **6**, 33086 (2016).

[60] E. Y. Sidky and X. Pan, Phys. Med. Biol. **53**, 4777 (2008).

[61] T. L. Jensen, J. H. Jørgensen, P. C. Hansen, and S. H. Jensen, BIT Numer. Math. **52**, 329 (2012).

[62] M. Abir, F. Islam, D. Wachs, and H.-K. Lee, J. Radioanal. Nucl. Chem. **307**, 1967 (2016).

[63] D. Kazantsev, W. M. Thompson, W. R. B. Lionheart, G. V. Eyndhoven, A. P. Kaestner, K. J. Dobson, P. J. Withers, and P. D. Lee, Inverse Probl. Imaging **9**, 447 (2015).

[64] D. Kazantsev, G. Van Eyndhoven, W. R. B. Lionheart, P. J. Withers, K. J. Dobson, S. A. McDonald, R. Atwood, and P. D. Lee, Philos. Trans. R. Soc., A **373**, 20140389 (2015).

[65] J. S. Jørgensen and E. Y. Sidky, Philos. Trans. R. Soc., A **373**, 20140387 (2015).

[66] J. S. Jørgensen, S. B. Coban, W. R. B. Lionheart, S. A. McDonald, and P. J. Withers, Meas. Sci. Technol. **28**, 124005 (2017).

[67] S. A. McDonald, P. M. Mummery, G. Johnson, and P. J. Withers, J. Microsc. **223**, 150 (2006).

[68] E. Bele, A. Goel, E. G. Pickering, G. Borstnar, O. L. Katsamenis, F. Pierron, K. Danas, and V. S. Deshpande, J. Mech. Phys. Solids **102**, 80 (2017).

[69] O. O. Taiwo, D. P. Finegan, J. M. Paz-Garcia, D. S. Eastwood, A. J. Bodey, C. Rau, S. A. Hall, D. J. L. Brett, P. D. Lee, and P. R. Shearing, Phys. Chem. Chem. Phys. **19**, 22111 (2017).

[70] C. Jailin, A. Buljac, A. Bouterf, M. Poncelet, F. Hild, and S. Roux, Meas. Sci. Technol. **29**, 024003 (2018).

[71] U. Hampel, A. Bieberle, D. Hoppe, J. Kronenberg, E. Schleicher, T. Sühnel, F. Zimmermann, and C. Zippe, Rev. Sci. Instrum. **78**, 103704 (2007).

[72] L. Ritschl, S. Sawall, M. Knaup, A. Hess, and M. Kachelrie, Phys. Med. Biol. **57**, 1517 (2012).

[73] S. L. Fisher, D. Holmes, J. S. Jørgensen, P. Gajjar, J. Behnsen, W. R. B. Lionheart, and P. J. Withers, "Laminography in the lab: Imaging planar objects using a conventional x-ray CT instrument," Meas. Sci. Technol. (submitted).